



**HAL**  
open science

## Design and commissioning of a neutron counter adapted to high-intensity laser matter interactions

V. Lelasseux, P.-A. Söderström, S. Aogaki, K. Burdonov, M. Cerchez, S. Chen, S. Dorard, A. Fazzini, M. Gugiu, S. Pikuz, et al.

### ► To cite this version:

V. Lelasseux, P.-A. Söderström, S. Aogaki, K. Burdonov, M. Cerchez, et al. Design and commissioning of a neutron counter adapted to high-intensity laser matter interactions. *Review of Scientific Instruments*, 2021, 92, 10.1063/5.0057828 . insu-03717913

**HAL Id: insu-03717913**

**<https://insu.hal.science/insu-03717913>**

Submitted on 21 Nov 2022

**HAL** is a multi-disciplinary open access archive for the deposit and dissemination of scientific research documents, whether they are published or not. The documents may come from teaching and research institutions in France or abroad, or from public or private research centers.

L'archive ouverte pluridisciplinaire **HAL**, est destinée au dépôt et à la diffusion de documents scientifiques de niveau recherche, publiés ou non, émanant des établissements d'enseignement et de recherche français ou étrangers, des laboratoires publics ou privés.

# Design and commissioning of a neutron counter adapted to high intensity laser matter interactions

V. Lelasseux,<sup>1, a)</sup> P.-A. Söderström,<sup>2, b)</sup> S. Aogaki,<sup>2</sup> K. Burdonov,<sup>1, 3, 4</sup> M. Cerchez,<sup>5</sup> S. N. Chen,<sup>2</sup> S. Dorard,<sup>1</sup> A. Fazzini,<sup>1</sup> M. Gugu,<sup>2</sup> S. Pikuz,<sup>6</sup> F. Rotaru,<sup>2</sup> O. Willi,<sup>5</sup> F. Negoita,<sup>2</sup> and J. Fuchs<sup>1</sup>

<sup>1)</sup>LULI - CNRS, CEA, UPMC Univ Paris 06 : Sorbonne Université, Ecole Polytechnique, Institut Polytechnique de Paris - F-91128 Palaiseau cedex, France

<sup>2)</sup>Extreme Light Infrastructure-Nuclear Physics (ELI-NP)/Horia Hulubei National Institute for Physics and Nuclear Engineering (IFIN-HH), Str. Reactorului 30, 077125 Bucharest-Măgurele, Romania

<sup>3)</sup>Sorbonne Université, Observatoire de Paris, Université PSL, CNRS, LERMA, F-75005, Paris, France

<sup>4)</sup>IAP, Russian Academy of Sciences, 603950, Nizhny Novgorod, Russia

<sup>5)</sup>Heinrich-Heine-Universität Düsseldorf | HHU · Institute of Laser and Plasma Physics, Universitätsstr. 1 40225 Düsseldorf, Germany

<sup>6)</sup>Russian Academy of Sciences | RAS · P. N. Lebedev Physical Institute, 53 Leninskiy Prospekt, 119991, Moscow, Russia

(Dated: 21 September 2021)

The advent of multi-PW laser facilities world-wide opens new opportunities for nuclear physics. With this perspective, we developed a neutron counter taking into account the specifics of a high intensity laser environment. Using GEANT4 simulations and prototype testings, we report on the design of a modular neutron-counter based on boron-10 enriched scintillators and high-density polyethylene moderator. This detector has been calibrated using a plutonium-beryllium neutron source and commissioned during an actual neutrons producing laser experiment at the LULI2000 facility (France). An overall efficiency of 4.37(59)% has been demonstrated during calibration with a recovery time of a few hundreds microseconds after laser-plasma interaction.

## I. INTRODUCTION

The objective of the work presented in this paper is the design and characterisation of a neutron detector to be used in experiments that exploit laser-driven particles or radiation to induce nuclear reactions. There are many advantages to laser-accelerated neutrons as they can be used to provide complementary data to measurements taken at traditional sources. Specifically, laser-driven sources provide high flux ( $> 10^{10}$  neutrons/shot<sup>1</sup>) in a short (picosecond<sup>2</sup>-nanosecond<sup>3</sup>) burst. We note that, with new laser facilities coming online over the next several years such as Apollon<sup>4</sup>, the Extreme Light Infrastructure (ELI) facilities ELI-Beamlines<sup>5</sup>, and ELI Nuclear Physics (ELI-NP)<sup>6-8</sup>, laser-driven neutron beams could open entirely new perspectives in nuclear physics, with possible flux reaching  $10^{24}$  neutrons/cm<sup>2</sup>/s per shot, see Ref.<sup>9</sup>.

In general, there are two basic approaches to detect neutrons: proton-recoil based detectors that are sensitive to fast neutrons and capture-reaction based detectors sensitive to neutrons with an energy close to room temperature. In laser-driven experiments aimed at detecting neutron beams, typically the first type of neutron diagnostics tools has been used, e.g. utilising proton recoils in plastic scintillators<sup>1,10</sup> or bubble dosimeters<sup>2,3,11</sup>. This type of system is typically characterised by low efficiency, but is satisfactory for the individual reconstruction of neutron events and their respective energies. The other capture-reaction-based type of detector

is based on a statistical counting where the neutrons emitted from the source are slowed down to thermal equilibrium with the ambient room environment, typically 0.025 eV in energy, in a high-density proton-rich material. Then, following the slowing down, the entire ensemble of neutrons is counted using a sensitive material with a large neutron-capture cross-section and a positive reaction  $Q$ -value. The positive reaction  $Q$ -value guarantees that all the neutrons captured will release the same amount of energy in the detector. Thus, the neutrons can be easily identified statistically from their energy deposition. One example of recent developments in this direction for laser-driven neutron diagnostics is Reference<sup>12</sup>, where a series of tubes filled with BF<sub>3</sub> gas was used as a sensitive volume, embedded in paraffin for moderation.

While the thermal neutron-capture method does not provide spectral information of the individual events, they are extensively used in the low-energy nuclear physics community for high-precision cross-section measurements of rare neutron-emitting reactions in astrophysics, medicine, and industrial applications. To reach a very high efficiency, the general approach for this type of design is to cover as much as possible surface area surrounding the reaction target with moderating material so that the neutrons, when emitted, will slow down independently of their emission direction. The sensitive parts of the detector should be placed as close as possible to a  $4\pi$  sr geometry in the moderating matrix. **In this kind of detector, it is important to optimise the distances between the detectors and the target, as well as the thickness of the moderating material the neutrons will experience. It is this optimisation that will be detailed in this paper. The paper is organized as follows. In Section II, we present the conceptual design of the detector, using GEANT4 simulations to define its overall**

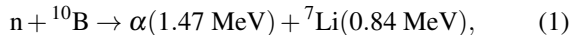
<sup>a)</sup>Electronic mail: vincent.lelasseux@polytechnique.edu

<sup>b)</sup>Electronic mail: par.anders@eli-np.ro

geometry, as well as the temporal evolution of the detected signal. Section II also reports on early testing at a laser facility of a prototype, in order to assess experimentally how such system can behave in the environment of an intense laser interacting with solid targets. In Section III, we report on the final design and calibration of the detector, which was optimized from that of the prototype. In Section IV, we report on preliminary results of the first full-scale use of the detector, as conducted at the LULI2000 laser facility. Section V summarizes the study.

## II. CONCEPTUAL DESIGN

The starting point for our laser-driven neutron-counter design followed the same line of reasoning as outlined in the discussion about neutron counters used in low-energy nuclear physics experiments. However, there is an additional constraints in laser-driven experiments, especially in light of the upcoming multi-PW era of laser-driven nuclear physics at Extreme Light Infrastructure – Nuclear Physics (ELI-NP) and Apollon laser facilities, namely the rather harsh environment, i.e. the high electromagnetic pulse (EMP) and the emission of other high energy radiation. For this reason, a part of the conceptual design was to search for a different solution compared to the regularly used, high-efficiency neutron counters, which consist of tubes filled with  $^3\text{He}$  gas or  $\text{BF}_3$  gas, and coupled with delicate pre-amplifier electronics that are very prone to picking up noise and would have a high chance not to survive the EMP. Therefore, we chose the plastic scintillator of type EJ-254 with a 1% loading of boron for detector material. In this case, the neutron sensitivity originates from the break-up of boron following thermal neutron capture via the reaction



releasing a total of  $Q = 2.31 \text{ MeV}$  of charged-particle kinetic energy and  $0.48 \text{ MeV}$  of  $\gamma$  energy in the scintillator material, producing scintillation photons. The emitted photons from the scintillator will allow us to use a photomultiplier tube (PMT) for signal readout instead of delicate pre-amplifiers, since the former have shown to perform well in high-power laser electromagnetic environments<sup>3,13</sup>. The scintillation properties of EJ-254 plastic scintillator, especially the light yield for both fast and thermal neutrons, have already been investigated by several teams<sup>14,15</sup>. We will not go here in the details of the scintillation properties of the detector, these being integrated in the final efficiency evaluation that will be detailed below. The scintillator-based detector will be encased in a moderator, in our case high-density polyethylene (HDPE), to slow down the produced MeV-range neutrons.

Another vital advantage of moderating the neutrons is that it should allow to cleanly count them without being hampered by the noise generated by the laser-matter interaction. Indeed, a typical moderation time in this type of HDPE is a few hundreds of microseconds. Thus, the neutrons will still arrive at the scintillator material well after the electromagnetic pulse, and the gammas generated by the prompt laser interaction with the primary target, have passed.

## A. GEANT4 simulations

### 1. Defining the detector geometry

The neutron detection method via moderation and neutron capture requires a large amount of material for moderation and detection. The experimental conditions at typical high power laser facilities make it such that space in the experimental chamber is limited since there is a significant amount of large optics and diagnostic equipment. An illustration of the commissioning experiment's spatial constraints, and of the final design of the present detector, is shown in Fig. 1. As can be seen, the detector cannot occupy the full space around the target since angular portions have to be carved out to leave room for laser beams and ancillary experimental detectors.

However for the sake of simplicity, we started the design of the detector by considering a simplified model having the form of a full cylinder. The value for the inner diameter is set to 40 cm to leave enough room for the target manipulator and other equipment near the target chamber centre. The height of the cylinder is limited to 60 cm due to a laser beam passing above the detector (see Fig. 1). Note that for simplicity, the full height is here occupied by the scintillator. All other dimensions were then left open for optimisation. A typical example of such geometry, where the outer radius is 65 cm, and having ten detector elements (containing the plastic scintillators+PMTs), is shown in Fig. 2. In this case, the solid angle subtended by the detector is 10 sr.

To determine the optimum detector geometry in its yet-unfixed dimensions, we used GEANT4<sup>16</sup>, a widely used Monte Carlo simulation toolkit developed by CERN to track particles through matter within high energy, nuclear and accelerator physics. The moderator material was chosen to be HDPE since it is well established as a neutron moderator and does not have significant out-gassing as to affect the vacuum properties of the interaction chamber<sup>17</sup>. The number of detectors (evenly distributed in the cylindrical volume, see Fig. 2), detector length, and outer radius of the moderator were all varied in the simulation. The results are presented in Fig. 4.

The simulations were performed based on the code developed for the BRIKEN project<sup>18–20</sup>, using the GEANT4 libraries version 10.5. The NeutronHP physics list was employed to get an accurate cross-section for the scattering of close-to-thermal neutrons, including molecular effects at a given temperature. The initial estimations were performed using 1 000 000 generated neutron events with monoenergetic distributions in steps of 100 keV ranging from 1 MeV up to 1.5 MeV over a wide range of geometric parameters. The chosen range for the neutron energies is inferred from the expected neutron spectrum shown in Fig. 3. This spectrum corresponds to the reaction  ${}^{51}\text{V}(p,n){}^{51}\text{Cr}$ .  ${}^{51}\text{V}$ , which is the main (p,n) reaction induced in natural V. The reaction is here triggered by a laser-induced proton beam, which is generated from a solid target by the Target Normal Sheath Acceleration (TNSA) mechanism<sup>21,22</sup>, characterized by a maximum (cutoff) energy of 16.8 MeV. Indeed, natural V is composed of 99.75% of  ${}^{51}\text{V}$  and 0.25% of  ${}^{50}\text{V}$ , and that reaction is the dominating reaction, due to its higher cross-section, for pro-

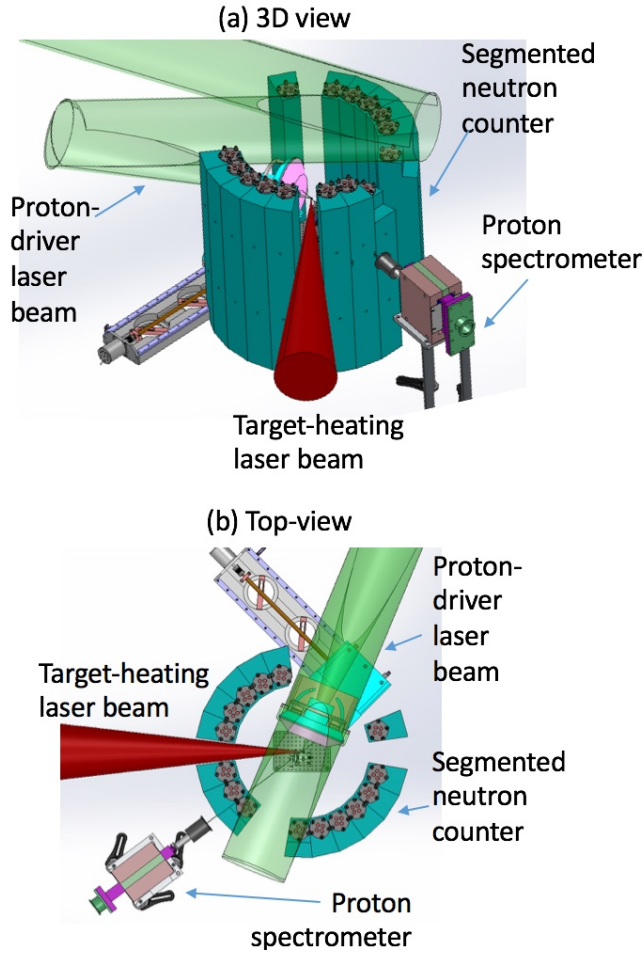


FIG. 1. Illustrations of the experimental design of the commissioning experiment utilising the neutron counter detailed in this paper, which is the segmented large array shown in dark green. The incoming laser beams are: the ps-duration, intense laser (shown in light green, transported and focused by large mirrors (not shown) inside the chamber) and the target-heating laser (in dark red). Additional major materials in the chamber are x-ray protection (pink) and proton spectrometry diagnostics.

tons having energies above 1.5 MeV, as commonly produced by high-intensity lasers<sup>9</sup>. This particular reaction was chosen for the experiment with the aim of studying electron screening effects in plasmas<sup>23</sup>, i.e. where one would study the yield of the (p,n) reaction in either a cold V target, or a heated one (by an auxiliary laser beam) to the plasma state<sup>24</sup>. In the case of the (p,n) reaction in V, the outgoing neutron spectrum will have a maximum between 1 and 1.5 MeV, as shown in Fig. 3.

The efficiencies shown in Fig. 4 correspond to the ratio  $E/N$ , where  $E$  is equal to the sum of the events corresponding to the total energy deposition of the nuclear break-up reaction of boron in the scintillating material by the  $\alpha$  particle and  ${}^7\text{Li}$  ion, and  $N$  is equal to the total amount of neutrons sent, in the simulation, to the detector. We selected those events, since, when we analyze the signal from the detector and plot the retrieved spectrum, we can identify (as will be detailed below) a

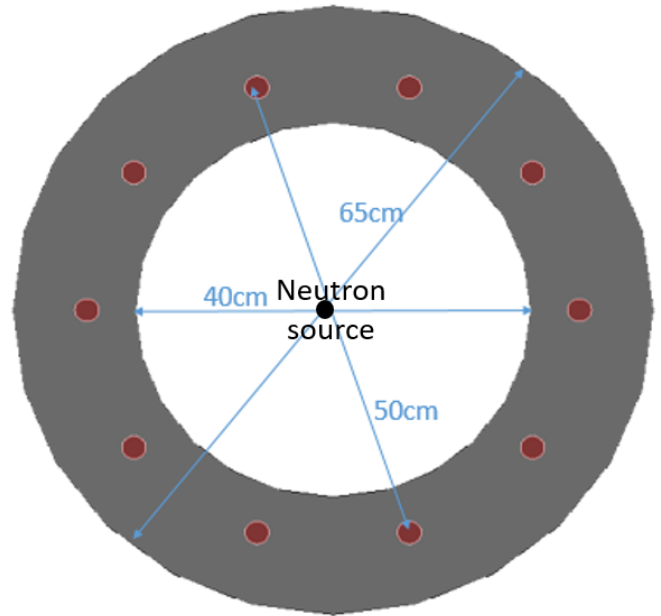


FIG. 2. Top-view of the GEANT4 model of the neutron counting system. This example contains 10 scintillators (in red) and a moderator volume (in grey) with an inner diameter of 40 cm and an outer diameter of 65 cm. Its height is 60 cm. Vertically, the neutron source is not at the center; it is positioned at 40 cm from the bottom and 20 cm from the top.

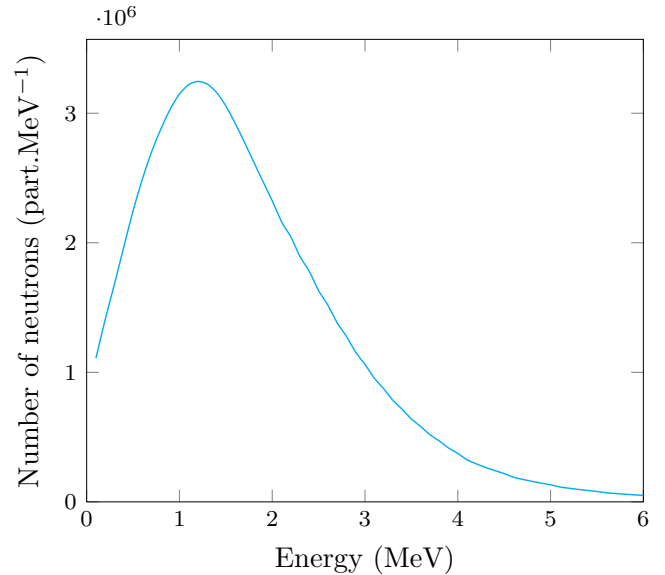


FIG. 3. Expected neutron spectrum produced by the  ${}^{51}\text{V}(p,n){}^{51}\text{Cr}$  reaction. The reaction is induced in natural V, which has 99.75% fraction of  ${}^{51}\text{V}$ , with the remaining 0.25% being  ${}^{50}\text{V}$ , by a laser-induced proton beam, generated from a solid target and by the TNSA mechanism<sup>3,21,22</sup>. That proton beam is modeled based on an experimentally measured beam. It is broadband, with a maximum (cutoff) energy of 16.8 MeV. The cross-section for the reaction was obtained from the TALYS database<sup>25,26</sup>.

peak in the spectrum around 100 keV<sub>ee</sub>, which can only be as-

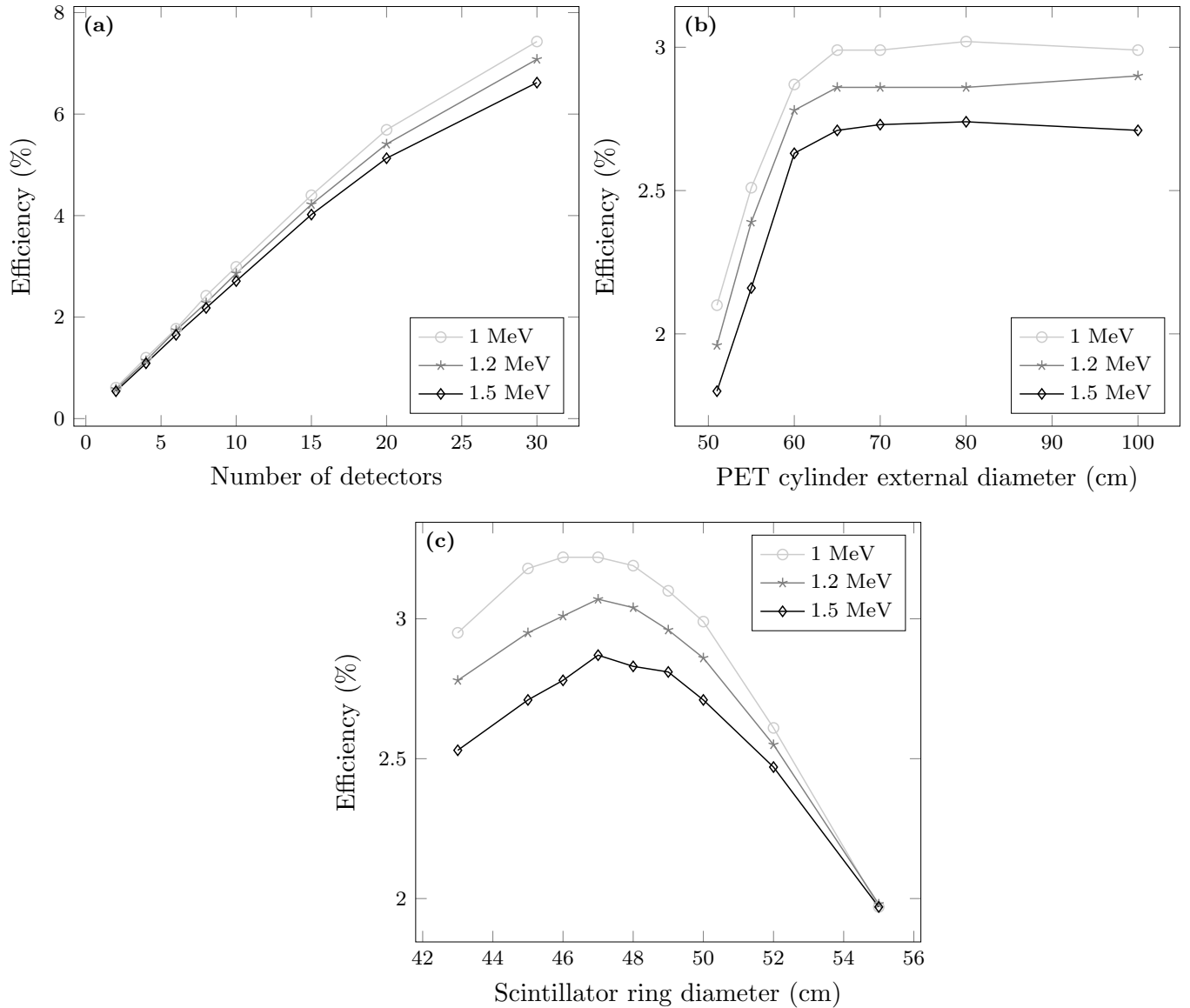


FIG. 4. Simulated neutron detection efficiency (in %, see text for definition) of an idealised full array (as shown in Fig. 2) for several neutron energies (we use here monochromatic neutrons as input) and (a) as a function of the number of scintillators distributed in the moderator, (b) the external diameter of the moderator cylinder, and (c) the diameter of the circle on which the scintillators are placed. The basic parameters for those calculations are a height of 60 cm, an internal diameter of 40 cm, an external diameter of 65 cm, a scintillator circle diameter of 50 cm and ten scintillators.

sociated with that break-up. Hence, since we will later isolate the signal as the one participating to this peak, we will count for the efficiency only those events corresponding to the total energy deposition of the nuclear break-up. The variation of the efficiency as a function of the number of detector units within the whole detector is shown in Fig. 4.a.

Fig. 4.a shows that, as we would expect, the overall efficiency increases linearly with the number of detectors until 15 or so. Afterwards, the gain in efficiency as we increase the number of detector becomes less important. Thus, we have decided on using 15 detectors in the whole detector. Fig. 4.b shows the amount of HDPE needed to **thermalize as many as**

**possible** neutrons of interest: we observe that the efficiency plateaus if the HDPE cylinder is thicker than 25 cm thickness, this being due to the useful neutrons being already **thermalized** in the HDPE, there is no need to have a thicker thermalizing medium.

Fig. 4.c displays the efficiency estimation as a function of the position of the individual detector units (comprising the scintillators+PMTs) within the HDPE matrix. From it, we can infer that the efficiency reaches a peak around when the detectors are positioned around 48 cm in radius.

In summary, in this ideal case with no noise and a 100% efficiency for the PMTs, these simulations give us a neutron-

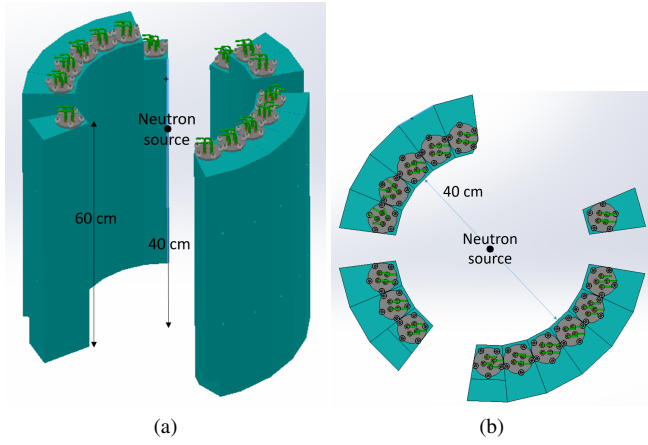


FIG. 5. Sketch of the chosen setup with 15 modular pieces.

counting efficiency of a few percents. Due to the positive  $Q$ -value of the detection reaction, there is no low-energy threshold, and our detector covers the full energy range of the neutrons produced. Based on Fig. 4, a solution consisting of 15 detector elements was chosen. In the final design, the detector has a "cheese wedge" feature such that sections can be taken out to accommodate laser and detector paths and make the whole detector modular. It has an inner diameter of 40 cm, an outer diameter of 65 cm, a height of 60 cm and the scintillators are placed on a circle with a 48 cm diameter. Fig. 5 shows a sketch of this final setup. **This setup was used both for the calibration as well as for the LULI2000 experiments, both of which will be detailed below.** In this case, the solid angle subtended by the detector is 6.17 sr.

## 2. Time evolution study

With our design fixed, it is also interesting to study the time evolution of the energy deposition. This is especially important since EMP and other radiation should significantly impact our signal in the first  $\mu\text{s}$  after the laser shot. To do so, we built in our simulation a more accurate representation of the final design as shown in Fig. 6.

When filtering events to get only energy deposition corresponding to the  $Q$ -value peak, we have been able to get the time evolution of neutron detection as shown in Fig. 7. We note that the signal peaks after around 1  $\mu\text{s}$ , which is related to the time it takes for neutrons to be moderated in the HDPE. The temporal evolution of the energy deposition can be fitted with a sum of two exponentials, as shown. The first one has a half-life value around 10  $\mu\text{s}$  and the second one around 100  $\mu\text{s}$ . This knowledge will allow us to extrapolate the number of neutrons arriving onto the detector, based on the fraction that can be detected after the black-out period, of tens of  $\mu\text{s}$  (see below), after the laser shot.

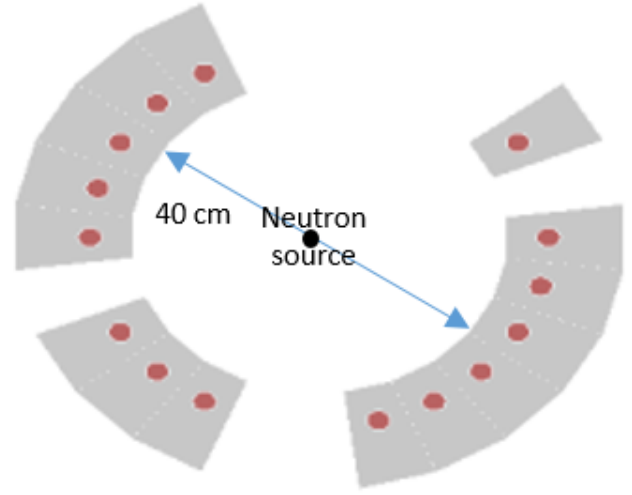


FIG. 6. Representation of the GEANT4 model used for the time evolution study.

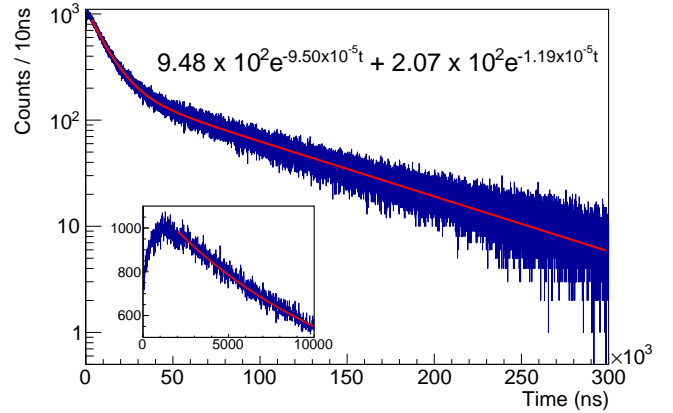


FIG. 7. Evolution of the neutron detection for the neutron spectrum displayed in Fig. 3, over the first 300  $\mu\text{s}$ . Inset: Zoom-in over the first 10  $\mu\text{s}$ , showing that the signal peaks around 1.2  $\mu\text{s}$ . **The axes of the inset represent the same values, in the same units, as the main graph.**

## B. Prototype testing

A prototype detector unit was built to test the design, **especially in a laser environment**, and debug the system. One detector was constructed, as shown in Fig. 8. It consisted of a 50 mm long plastic scintillator with a 30 mm diameter. The scintillator was connected to two PMTs (**model PMS XP2972 from Philips**), one on each end, where one of the PMTs was loaded with a spring to keep a firm connection between the scintillating material and the readout. The setup was enclosed in a vacuum-tight and light-tight aluminium housing, forming an air-lock around the detector components.

The prototype detector was evaluated using a standard  $^{137}\text{Cs}$   $\gamma$ -ray source, as well as plutonium-beryllium (PuBe) **neutron** source with a well-characterised energy

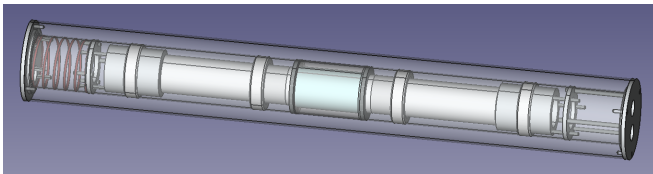


FIG. 8. Drawing of the prototype detector with a 50 mm long cylindrical plastic scintillator (shown in turquoise) between two photomultiplier tubes. One of the photomultiplier tubes is connected with a spring to the outside wall to keep a solid connection.

distribution<sup>27</sup>. These evaluations consisted in determining the  $\gamma$ -ray response, neutron response, and digital electronic read-out for feasibility to use within actual experimental conditions. One of the critical aspects of these measurements was to evaluate a two-PMTs readout concept, namely in coincidence counting mode. The PMTs were biased with a high voltage of 1.2 kV and read out using CAEN VX1730B digitiser units with a sampling frequency of 500 MS/s and a resolution of 14 bits, operated with Digital Pulse Processing - Pulse Shape Discrimination (DPP-PSD) firmware version 4.17.

The  $\gamma$ -ray response was evaluated using a 313 kBq  $^{137}\text{Cs}$  source placed directly at the detector wall that provided  $\gamma$  rays with an energy of 661.66 keV, giving a Compton edge in the energy distribution measured in the detector system at 477.34 keV. The  $^{137}\text{Cs}$   $\gamma$ -ray source was placed next to the scintillator in the middle of the assembly.

For the energy calibration, the  $^{137}\text{Cs}$  Compton edge location was taken to be at 80% height on the high-energy side of the  $\gamma$ -ray distribution, in line with the findings reported for low-Z scintillators measured in coincidence with a high-purity germanium detector<sup>28</sup>. A typical, calibrated,  $\gamma$ -ray energy spectrum is shown in Fig. 9.a.

As shown in Fig. 9, the two PMTs gave a very similar individual response. Furthermore, we also show the energy spectrum where we require a signal from both PMTs to be coincident within a time window of 5 ns, and each event's energy is taken as the sum of the light measured by both PMTs. This spectrum, also shown in Fig. 9, is entirely consistent with the energy spectrum of the individual PMTs, with a slightly lower low-energy noise, and almost no positive events are lost in the coincidence counting mode of operation.

To evaluate the neutron response of the prototype scintillator, we used a PuBe neutron source with a moderator. The full characteristics of this source have already been reported in Söderström et al.<sup>27</sup>. This source produced  $2.22 \times 10^5$  neutrons per second with a mean energy of 3.25 MeV and a maximum energy around 12 MeV. The PuBe neutron source was placed at a distance of 30 cm from the detector unit and the emitted neutrons were moderated using 10 cm of HDPE placed in between. Also, we placed 5 cm of lead in front of the detector to reduce the influence of 4.4 MeV  $\gamma$  ray of  $^{12}\text{C}$  that is occasionally produced in the PuBe reaction. Performing the same exercise as with the  $^{137}\text{Cs}$  data, we constructed the energy spectrum for the individual PMTs with the coincidence requirement. We show these results in Fig. 9.b. The most notable features in this spectrum are that the background noise

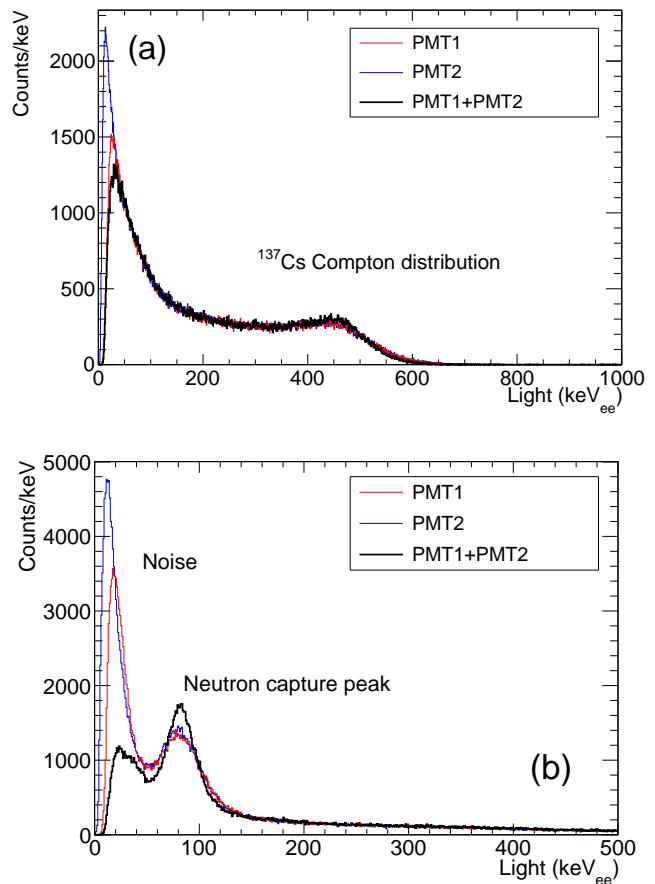


FIG. 9. Histogram of the light collected by the prototype detector consisting of two PMTs, as collected with a  $^{137}\text{Cs}$   $\gamma$ -ray source (top) and a PuBe neutron source (bottom). The blue and red histograms correspond to the individual PMTs, while the black histogram corresponds to events coincident in both PMTs. The recorded light in both cases has been calibrated in keV electron equivalent energy using the location of the  $^{137}\text{Cs}$  Compton edge.

is heavily reduced with the coincidence requirement and that the neutron-capture peak becomes significantly more prominent. In total, we obtain the mean value of the neutron-capture peak at an energy of 83.81(11) keV<sub>ee</sub> with an energy resolution of the detector unit of 28.55 keV<sub>ee</sub> full width at half maximum (FWHM). This value is significantly lower than the reaction  $Q$ -value and reflects the loss of energy from the initial products ( $\alpha$  particle and  $^7\text{Li}$ ) to the emitted photons. It is, however, well above the detector noise and provides a very clean neutron signal.

### C. Dusseldorf test

To test the response of the detector to prompt  $\gamma$ -rays generated during the laser-matter interaction and the impact of the EMP and radiation noise, the prototype scintillator-PMT assembly was installed at an experimental campaign where thin titanium foils were shot at the ARCTURUS laser (30 fs,  $10^{20}$

$\text{W}/\text{cm}^2$ ) of the Heinrich Heine Universität of Düsseldorf. The assembly was put horizontally 30 cm away from the target chamber centre and 15 cm below the equatorial plane.

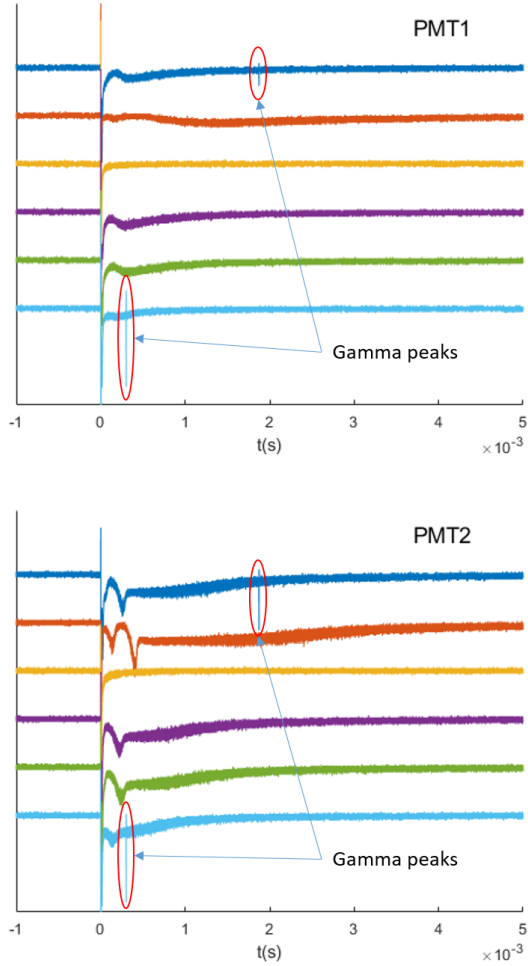


FIG. 10. Readout signal detected on a prototype scintillator-PMT assembly during a test campaign conducted at the ARCTURUS laser. We can see here the evolution of the two PMTs output voltage over 5 ms during six shots, which are each vertically shifted with respect to the others, for clarity.

Fig. 10 shows the voltage signal output by the PMTs as a function of time. We see in the first (top) trace, as well as in the last (bottom) trace, an isolated peak. These are seen both in PMT1 and PMT2, and are correlated in time between the two PMTs. They thus clearly correspond to a real energy deposition from a gamma-ray reflecting from the environment of the target area and entering late into the detector. We also observe, as shown in Fig. 10, that during the first few  $\mu\text{s}$ , there is fast, large-amplitude oscillations due to the prompt EMP,  $\gamma$ -rays and x-rays. After this period, over a few hundreds of  $\mu\text{s}$  the base-line of the signal returns to zero, thus a detector counting moderated neutrons should function correctly at this time.

We should note that the laser pulse duration on this facility was only 30 fs. Hence, these measurements are not neces-

sarily representative of the conditions taking place at facilities which have pulses of picosecond duration, which cause a larger EMP and gamma production. However, as the long-term aim of this instrument is for use at the Apollon and ELI-NP facilities, which have a pulse length of a few tens of fs, we expect these measurements at ARCTURUS to be more representative of the detector response in these conditions. It is, though, rather difficult to draw more precise conclusions from only these data since the EMP and gamma generation is very dependant on the facility parameters<sup>29,30</sup>.

In any case, apart from the first tens of  $\mu\text{s}$ , which are heavily perturbed, the base-line evolves much more slowly, which should not preclude the observation of the much shorter neutron deposition peaks, which are on the order of 10 ns duration.

### III. FINAL DESIGN

A view of the final detector unit is shown in Fig. 11. For the final system, the detectors consisted of plastic scintillators of type EJ-254 with 1% boron loading. Each element consisted of two 200 mm long EJ-254 rods with a diameter of 25.4 mm and diamond milled and polished edges. The plastic detectors were coupled into pairs, yielding a total length of 40 cm, as illustrated in Fig. 11. **The ensemble is wrapped in TYVEK high-reflectivity paper<sup>31</sup>. Note that compared to the conceptual design discussed in Section II, the total height of the detector is kept at 60 cm, 40 cm of which is occupied by the scintillator, the rest being occupied by the PMTs and connecting electronics.**

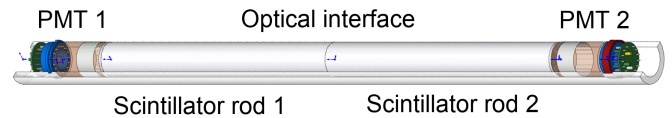


FIG. 11. Schematic drawing of a single active detector unit, consisting of two separate plastic scintillators and PMTs connected with an optical interface. Every single unit was encased in a thin HDPE shell to provide the necessary stability and a path for the signal and high-voltage cables to pass to the connectors.

**EJ-560 optical interface discs were used to couple the scintillators to each other and to the PMTs of model 9112B from ET Enterprise.** There is one PMT on each side of the assembly, with an active diameter of 22 mm, a 25% quantum efficiency at peak wavelength, an electron gain of  $10^6$ , a typical rise time of 1.8 ns and a transit time of 20 ns. The voltage to the PMTs was provided using C673A voltage dividers.

As shown in Fig. 12, the detector components were placed into individually manufactured HDPE shells providing the bulk of the moderator volume, as well as being vacuum-tight, thus serving as an air-lock for the PMTs. This modular design allows for the necessary flexibility to assemble the detector array in various configurations adapted to each experiment's particular requirements.

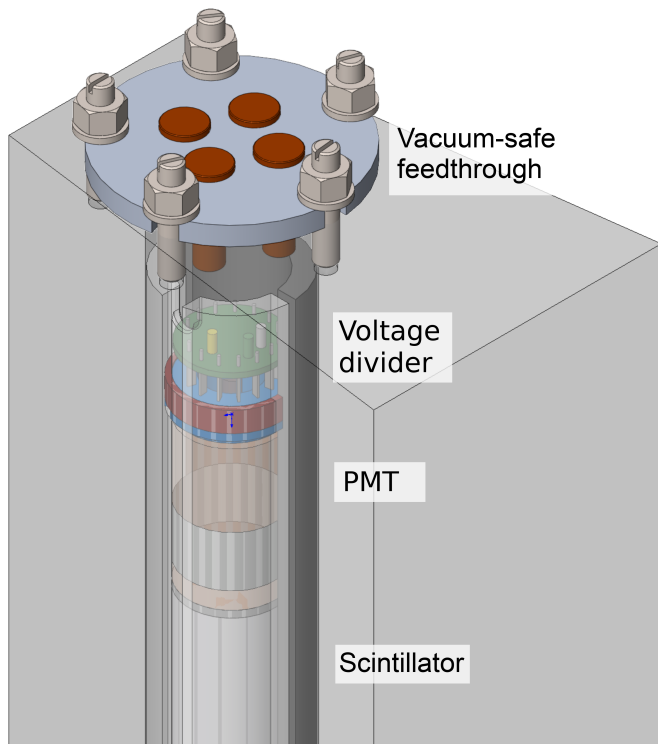


FIG. 12. Close up view of one of the final detector modules, showing the top part of the module with the end of the scintillator rod, the PMT and the voltage divider, and the arrangement for the vacuum sealing of the unit with the four LEMO feed-throughs connecting the signal and high-voltage cables to the top and bottom PMT.

For the first commissioning of the detector array, 15 detector modules were manufactured to be placed in the interaction chamber as shown in Fig. 5. A list of the individual detector properties is shown in Table I.

For the work presented in this paper, CAEN digitisers of type V1730 have been used, with a sampling frequency of 500 MS/s and a digital resolution of 14 bits.

### A. Neutron source measurements

The detector array was assembled and calibrated at the ELI-NP facility. **The calibration setup was exactly the same as shown in Fig. 5. The sources were placed at a 40cm height in the center of the detector.** The data signals were fed to a digital electronics system based on three CAEN V1730SB digitisers, consisting of 16 channels, each with a 14-bits resolution and a 500 MS/s sampling frequency. The boards were read out using a daisy chain of short optical fibre cables with the first and the last board connected via long optical fibres to a PCI express board installed in the data acquisition computer. The high-voltage to the PMTs was provided by two 24 channels CAEN A7030SN boards in a CAEN SY5527LC power supply system using cables with safe high voltage (SHV) to LEMO connectors, where the latter were connected to the PMTs.

The detector units' energy calibration was carried out using

TABLE I. The first 15 detector modules manufactured for the final neutron detector array, the angle defined in Fig. 6, and the high-voltage used for the individual PMTs.  $\theta$  is defined as the angle from the laser direction. Note that during this experiment, the PMT D08D showed a considerable leakage current and the entire module could not be operated during commissioning. In addition, we also list the location of the energy  $E$  of the neutron capture peak for each detector unit in keV electron equivalent and the width of the peak in % for the full-width at half-maximum. The efficiency of each unit is given with a PuBe neutron source as a reference.

ID	$\theta$ ( $^\circ$ )	PMT	HV (V)	$E$ (keV <sub>ee</sub> )	$\Delta E$ (keV <sub>ee</sub> )	$\epsilon$ (%)
D01	52.5	U D	1200 1200	95.6(37)	30.2(91)	0.030(17)
D02	82	U D	1000 1200	104.8(11)	43.2(33)	0.299(43)
D03	99.5	U D	1200 1200	114.9(11)	45.9(29)	0.320(40)
D04	114.5	U D	1200 1200	109.7(11)	42.9(24)	0.363(42)
D05	129.5	U D	1200 1200	119.9(20)	64.0(54)	0.402(57)
D06	144.5	U D	1200 1200	105.0(11)	43.7(25)	0.420(48)
D07	159.5	U D	1000 1200	104.7(15)	46.8(36)	0.359(51)
D08	202.5	U D	1200 -	-	-	-
D09	217.5	U D	1200 1200	110.0(12)	46.1(30)	0.338(43)
D10	232.5	U D	1200 1200	121.4(17)	66.6(63)	0.325(53)
D11	262.5	U D	1200 1200	99.9(12)	50.3(36)	0.366(47)
D12	277.5	U D	1200 1200	100.3(12)	49.3(34)	0.354(46)
D13	292.5	U D	1200 1200	99.7(10)	48.3(21)	0.365(35)
D14	307.5	U D	1200 1200	108.1(8)	35.8(19)	0.390(44)
D15	322.5	U D	1200 1200	99.3(50)	41(13)	0.039(22)

the same  $^{137}\text{Cs}$   $\gamma$ -ray source with an activity of 313 kBq at the time of measurement. Similarly, as for the prototype tests, the Compton edge location was taken to be at 80% height on the high-energy side of the  $\gamma$ -ray distribution. The data was collected using the CoMPASS data acquisition (DAQ) software and the DPP-PSD firmware installed on the digitiser cards, operated in internal-trigger mode. The Compton spectrum for the individual PMTs, as shown in Fig. 14, appears to exhibit a double edge structure. This peculiar structure might originate from the two-components construction, which is illustrated in Fig. 11, i.e. that comprises an imperfect intermediate optical interface. Indeed, such imperfections could reflect or absorb the light of each event asymmetrically, letting appear two Compton edges.

To calibrate in energy each of the two PMTs, we used the Compton edge located at high energy (477.34 keV) as a ref-

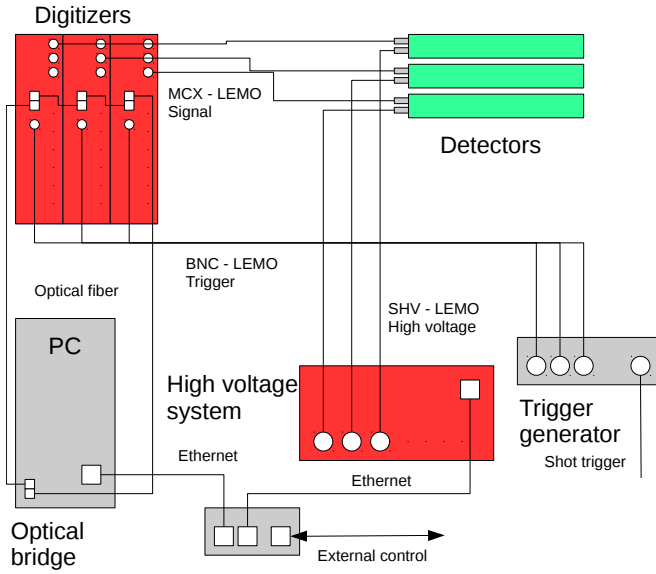


FIG. 13. Schematic illustration of typical hardware infrastructure for the operation of the detector array discussed in this work. For the LULI2000 commissioning, the digitisers were of type CAEN V1730SB, read out via the A3818 optical bridge, and the high-voltage system consisted of A7030SN cards in an SY5527LC main-frame.

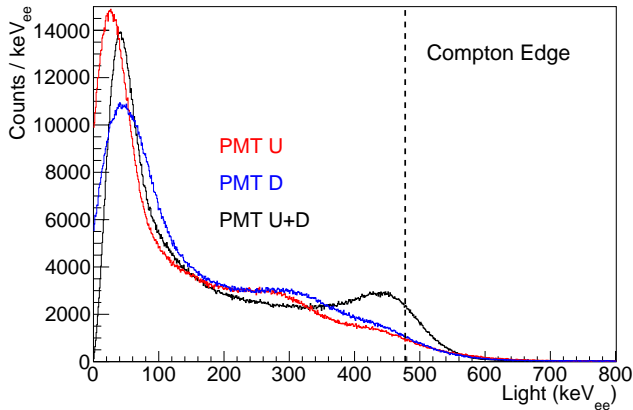


FIG. 14. Histogram of the light collected by the two individual PMTs of detector unit 7 (red up, blue down) using a  $^{137}\text{Cs}$   $\gamma$ -ray source, with an approximate energy calibration. The black histogram shows the sum of the two PMT signals re-calibrated to the Compton edge energy at 80% height of the Compton distribution, highlighted as a dashed black line.

erence point since it corresponds to the maximum energy that can be deposited in the scintillator by a 661.66 keV gamma (released by a  $^{137}\text{Cs}$ ) and scattered in the scintillator. After this preliminary calibration, the two signals were summed together for each coincident event and re-calibrated against that same 477.34 keV Compton edge. The obtained, final, energy spectrum clearly shows the typical structure of a Compton distribution with a well defined Compton edge.

To verify that the double structure did indeed originate from

a position dependence in the interaction, we tested the response of the two PMTs (of detector unit #4) to the location of the energy deposition along the unit. This was done using the very same  $^{137}\text{Cs}$  gamma source, which was this time positioned behind a lead collimator having a 1 cm hole, so that the angular emission of the gammas could be narrowed down. Five different positions have been investigated, as shown in the sketch of Fig. 15. For clarity, only the results for position 2, 3 and 4 will be shown.

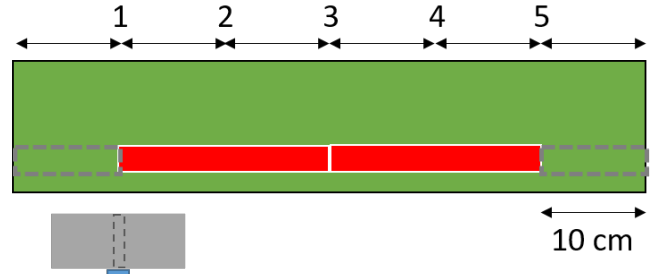


FIG. 15. Drawing of the setup of the measurement conducted to test the dependence (in the detector unit) of the light collected by the PMTs positioned at each end, with respect to the localisation of the energy deposition in the scintillator unit. The  $^{137}\text{Cs}$  gamma source is shown in blue. It is located behind a collimator composed of a lead brick (shown in grey), having a central hole with a diameter 1 cm. The source is here shown in position 1. In green is a detector unit, where is represented in red the position of the two segments composing the scintillator. At each end of those segments, the grey dotted rectangles represents the localisation of the PMTs and electronic parts. The location of the PMTs and connecting electronics is represented by the dotted rectangle at the end of the scintillator. The numbers represent the 5 positions where the source has been placed successively for the measurement.

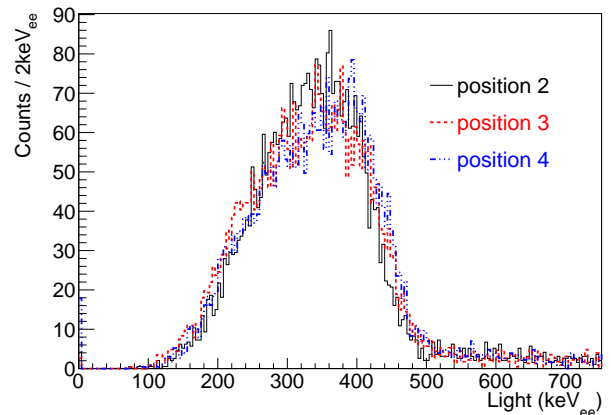


FIG. 16. Histogram of the light collected by the detector unit when summing the energy measured by both PMTs for 3 different positions of the directive gamma source described in Fig. 15, and recalibrating the photon energy against the know Compton edge (477.34 keV). As one could expect, those spectra are identical.

Fig. 16 shows the response of each individual PMTs when moving the localised source along the detector, when Fig. 17

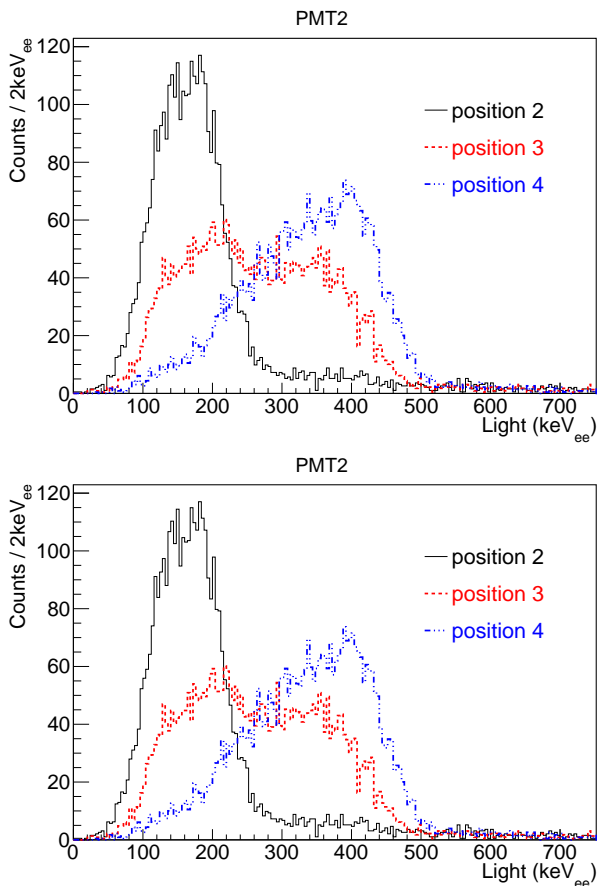


FIG. 17. Histogram of the light collected by the two PMTs (as labeled in Fig.15) of the detector unit #4, and for 3 different positions of the collimated gamma source (see Fig.15). We see that the amount of light collected by each PMT depends strongly on the position of the source.

shows the energy deposition when summing the energy obtained by both PMTs. Fig. 17 shows that the global response of the unit does not depend on the position of the interaction, which is reassuring for our energy calibration. However, when we look at the light received by each PMT in Fig. 16, there is a strong dependence of the signal seen by the two PMTs of the detector on the position of the source: when the source is located in front of one segment of the scintillator, the PMT attached to that segment sees a strong (energetically speaking) signal whereas the PMTs attached to the other segment sees a weak signal. Moreover, the spectra recorded for position 3 (both for PMT1 and 2) have two contributions. One could even guess that the source was not exactly centered and a bit on the PMT2 side. All those hints seem to confirm that the amount of light detected by each PMT is asymmetric and depends on which segment of the overall scintillating assembly the energy deposition takes place in.

For the calibration using the neutron-emitting PuBe source, we used a 1 Hz pulser as the external trigger to mimic the external trigger used in laser experiments and the digitisers' entire recorded signals were read out as complete waveforms for a defined time (1 ms) and analysed off-line on a shot-by-

shot basis.

We used the DPP-PSD firmware with waveform writing output mode to accommodate this. In this configuration, the digitiser cards were operated by the Waveform Recording Firmware, and the internal memory buffer was modified to contain at least  $5 \times 10^5$  sampling points, corresponding to 1 ms of waveform length. The readout was done using a dedicated DAQ with a custom data collection and analysis software, where the control of the digitisers was implemented via the CAEN digiTES framework. The record length for each waveform following a trigger was set to 992 ns. In Fig. 18, a histogram showing the typical variation of the waveforms selected on detector energy deposition corresponding to neutron-capture energies is shown, together with one typical waveform showing the level of noise in the detector. From

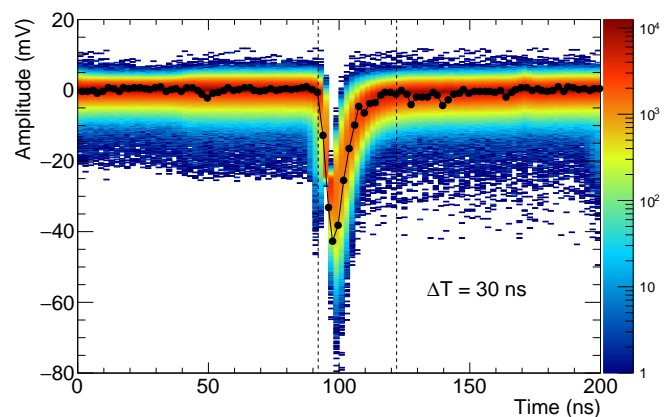


FIG. 18. Typical detector pulse shape shapes following the capture of thermal neutrons collected from detector 7. The colour histogram accumulates  $\sim 150000$  wave-forms and the black connected line one single typical wave-form. Black circles show the individual sampling points.

this, we can see that a typical integration time of around 30 ns should be enough to cover a good neutron-capture event completely. A neutron signal is, furthermore, seen to have an amplitude of approximately 50 mV.

A typical neutron energy spectrum retrieved following this procedure is shown in Fig. 19. For this calibration, 736 sets of traces were registered. The integral of the fitted Gaussian was then divided by the total duration of the recorded set which is 0.736 s and the neutron production of the source which is  $2.22 \times 10^5$  neutrons per second, to finally get an efficiency for each unit. Of course, this efficiency depends on the neutron energy spectrum. Depending on the experiment and the actual neutrons the detector will be exposed to, simulations will be needed to correct this efficiency and adapt it to the energy spectrum of the neutrons which are measured.

#### IV. LULI2000 EXPERIMENT

The commissioning experiment of the detector system was carried out at the LULI200 facility. The detector arrangement,

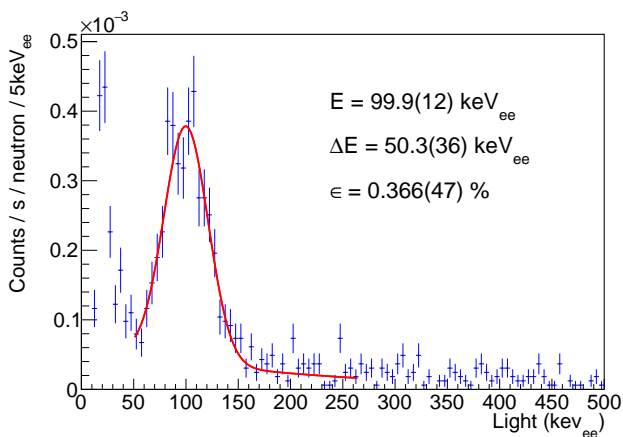


FIG. 19. Measured histogram (blue crosses) of the light collected by the detector 11 using a PuBe neutron source, external trigger and off-line pulse-shape analysis. The histogram only contains those events where both PMTs generated a realistic neutron signal. The red line corresponds to a Gaussian plus exponential fit to the data. From the fitted area, we can extract a neutron detection efficiency of 0.366% for this particular detector, with the neutron-capture energy peak located at 99.9 keV, with an FWHM resolution of 50.3 keV.

as shown in Fig. 1, was placed in the MILKA chamber where a 40 J laser, 1 ps beam was focused on the proton generating target. The protons were produced by the Target Normal Sheath Acceleration (TNSA) mechanism, which has been investigated in detail and is well documented<sup>21,22,32</sup>. The continuous energy spectrum of the proton is characterized on every shot using a magnetic spectrometer. This first target was a 23  $\mu\text{m}$  plastic foil for the acceleration of protons and a 1  $\mu\text{m}$  foil of natural vanadium to 99.75% of the  $^{51}\text{V}$  isotope was the secondary target, which was positioned 500  $\mu\text{m}$  after the primary target.

The typical electronics setup shown in Fig. 13 was prepared for this measurement. To trigger the system, the laser trigger signal was used, split between three digitiser modules using a Stanford Research Systems DG535 gate generator, and delayed such that it would provide approximately 100 ns worth of sampling points before the laser interaction with the target. A typically recorded waveform from one of the detectors, detector unit #12, is shown in Fig. 20 for the two PMTs separately. A few distinct features can easily be noticed in this figure. Immediately after the laser shot, there is a strong EMP signal; the detector is unresponsive for a brief period of time and we begin to count when the peak density, i.e. the number of detected event as a function of time, reaches a maximum which is here 140  $\mu\text{s}$  after the EMP.

For the analysis of the time series waveforms, namely counting the individual neutron signals, a software leading-edge discriminator was implemented with a threshold of  $\sim 4.75$  mV for the upper PMT, and  $\sim 3.75$  mV for the lower PMT, well below the expected neutron signal. While these values are for the particular traces shown in Fig. 20, they will change from detector unit to detector unit. We optimized the thresholds such that we can observe a clear peak in the spec-

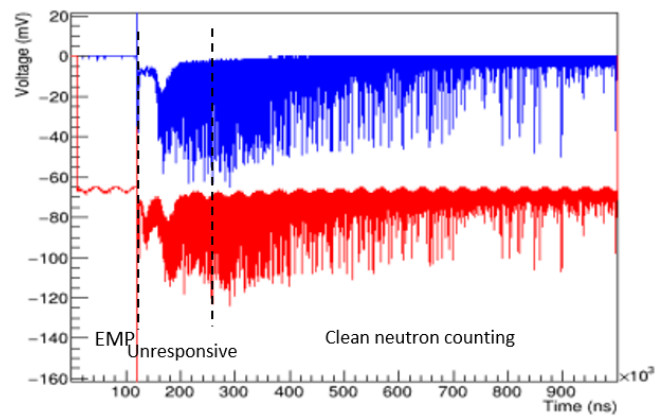


FIG. 20. Example of two waveforms from detector unit #12 following a laser shot on a proton and unheated vanadium target. The upper PMT is shown as a red waveform, and the lower PMT is shown as a blue waveform. Note that the red waveform is affected by a small amplitude modulation that originates from a defect in the acquisition card. The time of the EMP associated with the laser shot has been highlighted. The region where a clean neutron counting can be performed is highlighted as well.

trum around 100 keV as shown in Fig. 21, while maximizing the number of detected neutron events.

To identify each individual peak, for each time-step, we first define a baseline as the mean of the signal during the preceding 80 ns (i.e. twice the average duration of an individual peak), then we check if the signal exceeds the baseline by at least the threshold. If this is the case, we identify the maximum height of the signal, subtracting the baseline, over the following 40 ns. Then we define the individual peak by the temporal window around that maximum for which the signal height is at least equal to 10% of the maximum height. We can now integrate in time that individual peak to get an amount of light collected, using the adequate coefficient defined during the energy calibration process. When operating in coincidence mode, a window of 10 ns between the upper and lower PMT was used and any signal that did not have an equivalent signal by its paired PMT within this window is rejected. In the resulting spectrum shown in Fig. 21, a peak approximately corresponding to the light output expected from neutron capture events in the scintillator can be seen from the shot with the neutron-producing target, while the shot without the neutron-producing target does not exhibit a similar peak.

## V. SUMMARY AND CONCLUSIONS

We have presented the process of designing and constructing a neutron counter for use in high-power laser environments. The procedure reported here includes detailed simulations of detector properties, prototype testing, software development and hardware for readout, and finally, a commissioning test of the final detector units under realistic conditions. To conclude, neutron events can be selected and separated from the very noisy environment induced by the laser-matter inter-

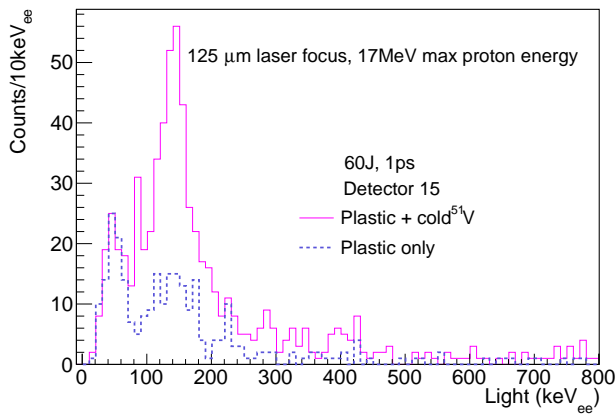


FIG. 21. Histogram of the light collected by the detector unit #15 for two different shots. One shot was conducted using solely a proton-generating plastic target exposed to the ps-duration intense laser (full line). The second shot was conducted using the same target, followed by a V solid converter (dashed line). The light output shown here is accounted from the sum of the two PMTs, re-calibrated against the Compton edge of a  $^{137}\text{Cs}$  source. The light peak corresponding to neutron capture in boron, which is expected to be around 100 keV, is clearly present in the neutron-producing shot using the V converter.

action. By taking advantage of the delay due to moderation, the electronics had time to recover from the noisy laser-solid interaction and therefore, the detectors were able to collect the neutron signal. Furthermore, we note that this type of detector can also be used in Time-Of-Flight configuration without the HDPE<sup>33</sup>.

## ACKNOWLEDGMENTS

The authors would like to thank the teams of IFIN-HH and ELI-NP (Romania), as well as LULI (France) for their expert technical support. We also acknowledge the support from the Extreme Light Infrastructure Nuclear Physics (ELI-NP) Phase II, a project co-financed by the Romanian Government and the European Union through the European Regional Development Fund - the Competitiveness Operational Programme (1/07.07.2016, COP, ID 1334), and by the project *ELI-RO-2020-23* funded by IFA (Romania). This work was also supported by funding from the European Research Council (ERC) under the European Unions Horizon 2020 research and innovation program (Grant Agreement No. 787539).

## DATA AVAILABILITY

Raw data were generated at the LULI2000 large scale facility. Derived data supporting the findings of this study are available from the corresponding author upon reasonable request.

## REFERENCES

- <sup>1</sup>M. Roth, D. Jung, K. Falk, N. Guler, O. Deppert, M. Devlin, A. Favalli, J. Fernandez, D. Gautier, M. Geissel, R. Haight, C. E. Hamilton, B. M. Hegelich, R. P. Johnson, F. Merrill, G. Schaumann, K. Schoenberg, M. Schollmeier, T. Shimada, T. Taddeucci, J. L. Tybo, F. Wagner, S. A. Wender, C. H. Wilde, and G. A. Wurden, “Bright laser-driven neutron source based on the relativistic transparency of solids,” *Phys. Rev. Lett.* **110**, 044802 (2013).
- <sup>2</sup>I. Pomerantz, E. McCary, A. R. Meadows, A. Arefiev, A. C. Bernstein, C. Chester, J. Cortez, M. E. Donovan, G. Dyer, E. W. Gaul, D. Hamilton, D. Kuk, A. C. Lestrade, C. Wang, T. Ditmire, and B. M. Hegelich, “Ultra-short pulsed neutron source,” *Phys. Rev. Lett.* **113**, 184801 (2014).
- <sup>3</sup>D. P. Higginson, L. Vassura, M. M. Gugu, P. Antici, M. Borghesi, S. Brauckmann, C. Diouf, A. Green, L. Palumbo, H. Petrascu, S. Sofia, M. Stardtubtsev, O. Willi, S. Kar, F. Negoita, and J. Fuchs, “Temporal narrowing of neutrons produced by high-intensity short-pulse lasers,” *Phys. Rev. Lett.* **115**, 054802 (2015).
- <sup>4</sup>D. N. Papadopoulos, J. P. Zou, C. Le Blanc, L. Ranc, F. Druon, L. Martin, A. Fréneaux, A. Beluze, N. Lebas, M. Chabanis, C. Bonnin, J. B. Accary, B. L. Garrec, F. Mathieu, and P. Audebert, “First commissioning results of the apollon laser on the 1 pw beam line,” *2019 Conference on Lasers and Electro-Optics (CLEO)*, , 1–2 (2019).
- <sup>5</sup>S. Weber, S. Bechet, S. Borneis, L. Brabec, M. Bučka, E. Chacon-Golcher, M. Ciappina, M. DeMarco, A. Fajstavr, K. Falk, E.-R. Garcia, J. Grosz, Y.-J. Gu, J.-C. Hernandez, P. J. M. Holec, M. Jantač, M. Jirka, H. Kadlecova, D. Khikhlikha, O. Klimo, G. Korn, D. Kramer, D. Kumar, T. Lastovička, P. Lutoslawski, L. Morejon, V. Olšovcová, M. Rajdl, O. Renner, B. Rus, S. Singh, M. Smid, M. Sokol, R. Versaci, R. Vrána, M. Vranic, J. Vyskočil, A. Wolf, and Q. Yu, “P3: An installation for high-energy density plasma physics and ultra-high intensity laser-matter interaction at ELI-Beamlines,” *Matter Radiat. Extremes* **2**, 149 (2017).
- <sup>6</sup>S. Gales, D. L. Balabanski, F. Negoita, O. Tesileanu, C. A. Ur, D. Ursescu, and N. V. Zamfir, “New frontiers in nuclear physics with highpower lasers and brilliant monochromatic gamma beams,” *Phys. Scr.* **91**, 093004 (2016).
- <sup>7</sup>S. Gales, K. A. Tanaka, D. L. Balabanski, F. Negoita, D. Stutman, O. Tesileanu, C. A. Ur, D. Ursescu, I. Andrei, S. Ataman, M. O. Cernianu, L. D’Alessi, I. Dancus, B. Diaconescu, N. Djourelou, D. Filipescu, P. Ghenuche, D. G. Ghita, C. Matei, K. Seto, M. Zeng, and N. V. Zamfir, “The extreme light infrastructure–nuclear physics (ELI-NP) facility: new horizons in physics with 10 PW ultra-intense lasers and 20 MeV brilliant gamma beams,” *Rep. Prog. Phys.* **81**, 094301 (2018).
- <sup>8</sup>K. A. Tanaka, K. M. Spohr, D. L. Balabanski, S. Balascuta, L. Capponi, M. O. Cernianu, M. Cucuic, A. Cucoanes, I. Dancus, A. Dhal, D. Dorria, P. Ghenuche, D. G. Ghita, S. Kisiov, V. Nastasa, J. F. Ong, F. Rotaru, D. Sangwan, P.-A. Söderström, D. Stutman, G. Suliman, O. Tesileanu, L. Tudor, N. Tsoneva, C. A. Ur, D. Ursescu, and N. V. Zamfir, “Current status and highlights of the ELI-NP research program,” *Matter Radiat. Extremes* **5**, 024402 (2020).
- <sup>9</sup>S. N. Chen, F. Negoita, K. Spohr, E. D’Humières, I. Pomerantz, and J. Fuchs, “Extreme brightness laser-based neutron pulses as a pathway for investigating nucleosynthesis in the laboratory,” *Matter Radiat. Extremes* **4**, 054402 (2019).
- <sup>10</sup>S. R. Mirfayzi, A. Alejo, H. Ahmed, D. Raspino, S. Ansell, L. A. Wilson, C. Armstrong, N. M. H. Butler, R. J. Clarke, A. Higginson, J. Kelleher, C. D. Murphy, M. Notley, D. R. Rusby, E. Schooneveld, M. Borghesi, P. McKenna, N. J. Rhodes, D. Neely, C. M. Brenner, and S. Kar, “Experimental demonstration of a compact epithermal neutron source based on a high power laser,” *Appl. Phys. Lett.* **111**, 044101 (2017).
- <sup>11</sup>Y. Arikawa, M. Utsugi, M. Alessio, T. Nagai, Y. Abe, S. Kojima, S. Sakata, H. Inoue, S. Fujioka, Z. Zhang, H. Chen, J. Park, J. Williams, T. Morita, Y. Sakawa, Y. Nakata, J. Kawanaka, T. Jitsuno, N. Sarukua, N. Miyana, M. Nakai, H. Shiraga, H. Nishimura, and H. Azechi, “High-intensity neutron generation via laser-driven photonuclear reaction,” *Plasma Fusion Res.* **10**, 2404003 (2015).
- <sup>12</sup>E. Guo, J. Chen, J. Xiong, Z. He, C. Wang, H. An, X. Huang, W. Wang, and J. Dong, “A neutron-diagnostic method using a  $\text{BF}_3$  detector array for ultrashort-pulse-laser neutron sources in strong gamma-ray environments,” *J. Instrum.* **14**, P10016 (2019).

- <sup>13</sup>M. Tarisien, J. L. Henares, C. Baccou, T. Bonnet, F. Boulay, F. Gobet, M. Gugiu, F. Hannachi, S. Kisyov, C. Manailescu, V. Meot, F. Negoita, X. Raymond, G. Revet, L. Tudor, and M. Versteegen, "Scintillators in high-power laser-driven experiments," *IEEE Trans. Nucl. Sci.* **65**, 2216 (2018).
- <sup>14</sup>G. Gabella, B. L. Goldblum, T. A. Laplace, J. J. Manfredi, J. Gordon, Z. W. Sweger, and E. Bourret, "Neutron response of the ej-254 boron-loaded plastic scintillator," *IEEE Transactions on Nuclear Science* **68**, 46–53 (2021).
- <sup>15</sup>Y. Sun, H. Zhang, X. Zhao, M. Shao, Z. Tang, and C. Li, "Identifying thermal neutrons, fast neutrons, and gamma rays by using a scintillator-based time-of-flight method," *Nuclear Instruments and Methods in Physics Research Section A: Accelerators, Spectrometers, Detectors and Associated Equipment* **940**, 129–134 (2019).
- <sup>16</sup>S. Agostinelli, J. Allison, K. Amako, J. Apostolakis, H. Araujo, P. Arce, M. Asai, D. Axen, S. Banerjee, G. Barrant, F. Behner, L. Bellagamba, J. Boudreau, L. Broglio, A. Brunengo, H. Burkhardt, S. Chauvie, J. Chuma, R. Chytraccek, G. Cooperman, G. Cosmo, P. Degtyarenko, A. dell'Acqua, G. Depaola, D. Dietrich, R. Enami, A. Feliciello, C. Ferguson, H. Fesefeldt, G. Folger, F. Foppiano, A. Forti, S. Garelli, S. Giani, R. Giannitrapani, D. Gibin, J. J. Gómez Cadenas, I. González, G. Gracia Abril, G. Greeniaus, W. Greiner, V. Grichine, A. Grossheim, S. Guatelli, P. Gumplinger, R. Hamatsu, K. Hashimoto, H. Hasui, A. Heikkinen, A. Howard, V. Ivanchenko, A. Johnson, F. W. Jones, J. Kallenbach, N. Kanaya, M. Kawabata, Y. Kawabata, M. Kawaguti, S. Kelner, P. Kent, A. Kimura, T. Kodama, R. Kokoulin, M. Kossov, H. Kurashige, E. Lamanna, T. Lampén, V. Lara, V. Lefebvre, F. Lei, M. Liendl, W. Lockman, F. Longo, S. Magni, M. Maire, E. Medernach, K. Minamimoto, P. Mora de Freitas, Y. Morita, K. Murakami, M. Nagamatu, R. Nartallo, P. Nieminen, T. Nishimura, K. Ohtsubo, M. Okamura, S. O'Neale, Y. Oohata, K. Paech, J. Perl, A. Pfeiffer, M. G. Pia, F. Ranjard, A. Rybin, S. Sadilov, E. di Salvo, G. Santin, T. Sasaki, N. Savvas, Y. Sawada, S. Scherer, S. Sei, V. Sirotenko, D. Smith, N. Starkov, H. Stoecker, J. Sulkimo, M. Takahata, S. Tanaka, E. Tcherniaev, E. Safai Tehrani, M. Tropeano, P. Truscott, H. Uno, L. Urban, P. Urban, M. Verderi, A. Walkden, W. Wander, H. Weber, J. P. Wellisch, T. Wenaus, D. C. Williams, D. Wright, T. Yamada, H. Yoshida, and D. Zschesche, "GEANT4—a simulation toolkit," *Nucl. Instrum. Methods Phys. Res. A* **506**, 250 (2003).
- <sup>17</sup>L. N. Dinh, J. Sze, M. A. Schildbach, S. C. Chinn, R. S. Maxwell, P. Raboin, and W. McLean II, "Vacuum outgassing of high density polyethylene," *J. Vac. Sci. Technol. A* **28**, 376 (2009).
- <sup>18</sup>A. Tarifeño-Saldivia, J. L. Tain, C. Domingo-Pardo, F. Calviño, G. Cortés, V. H. Phong, A. Riego, J. Agramunt, A. Algora, N. Brewer, R. Caballero-Folch, P. J. Coleman-Smith, T. Davinson, I. Dillmann, A. Estradé, C. J. Griffin, R. Grzywacz, L. J. Harkness-Brennan, G. G. Kiss, M. Kogimtzis, M. Labiche, I. H. Lazarus, G. Lorusso, K. Matsui, K. Miernik, F. Montes, A. I. Morales, S. Nishimura, R. D. Page, Z. Podolyák, V. F. E. Pucknell, B. C. Rasco, P. Regan, B. Rubio, K. P. Rykaczewski, Y. Saito, H. Sakurai, J. Simpson, E. Sokol, R. Surman, A. Svirikhin, S. L. Thomas, A. Tolosa, and P. Woods, "Conceptual design of a hybrid neutron-gamma detector for study of  $\beta$ -delayed neutrons at the RIB facility of RIKEN," *J. Instrum.* **12**, P04006 (2017).
- <sup>19</sup>J. L. Tain, J. Agramunt, D. S. Ahn, A. Algora, J. M. Allmond, H. Baba, S. Bae, N. T. Brewer, R. C. Folch, F. Calvino, P. J. Coleman-Smith, G. Cortes, T. Davinson, I. Dillmann, C. Domingo-Pardo, A. Estrade, N. Fukuda, S. Go, C. Griffin, R. Grzywacz, J. Ha, O. Hall, L. Harkness-Brennan, T. Isobe, D. Kahl, M. Karny, G. G. Kiss, M. Kogimtzis, A. Korgul, S. Kubono, M. Labiche, I. Lazarus, J. Lee, J. Liu, G. Lorusso, K. Matsui, K. Miernik, F. Montes, B. Moon, A. I. Morales, N. Nepal, S. Nishimura, R. D. Page, Z. Podolyak, V. F. E. Pucknell, B. C. Rasco, P. H. Regan, A. Riego, B. Rubio, K. P. Rykaczewski, Y. Saito, H. Sakurai, Y. Shimizu, J. Simpson, P. A. Söderström, D. W. Stracener, T. Sumikama, R. Surman, H. Suzuki, M. Takechi, H. Takeda, A. Tarifeño-Saldivia, S. L. Thomas, A. Tolosa-Delgado, V. Phong, and P. Woods, "The BRIKEN Project: Extensive Measurements of  $\beta$ -delayed Neutron Emitters for the Astrophysical r Process," *Acta Phys. Pol.* **B49**, 417 (2018).
- <sup>20</sup>A. Tolosa-Delgado, J. Agramunt, J. Tain, A. Algora, C. Domingo-Pardo, A. Morales, B. Rubio, A. T. no Saldivia, F. C. no, G. Cortes, N. Brewer, B. Rasco, K. Rykaczewski, D. Stracener, J. Allmond, R. Grzywacz, R. Yokoyama, M. Singh, T. King, M. Madurga, S. Nishimura, V. Phong, S. Go, J. Liu, K. Matsui, H. Sakurai, G. Kiss, T. Isobe, H. Baba, S. Kubono, N. Fukuda, D. Ahn, Y. Shimizu, T. Sumikama, H. Suzuki, H. Takeda, P. Söderström, M. Takechi, C. Bruno, T. Davinson, C. Griffin, O. Hall, D. Kahl, P. Woods, P. Coleman-Smith, M. Labiche, I. Lazarus, P. Morrall, V. Pucknell, J. Simpson, S. Thomas, M. Prydderch, L. Harkness-Brennan, R. Page, I. Dillmann, R. Caballero-Folch, Y. Saito, A. Estrade, N. Nepal, F. Montes, G. Lorusso, J. Liang, S. Bae, J. Ha, and B. Moon, "Commissioning of the BRIKEN detector for the measurement of very exotic  $\beta$ -delayed neutron emitters," *Nucl. Instrum. Methods Phys. Res. A* **925**, 133 (2019).
- <sup>21</sup>H. Daido, M. Nishiuchi, and A. S. Pirozhkov, "Review of laser-driven ion sources and their applications," *Reports on Progress in Physics* **75**, 056401 (2012).
- <sup>22</sup>A. Macchi, M. Borghesi, and M. Passoni, "Ion acceleration by superintense laser-plasma interaction," *Rev. Mod. Phys.* **85**, 751–793 (2013).
- <sup>23</sup>C. Spitaleri, C. Bertulani, L. Fortunato, and A. Vitturi, "The electron screening puzzle and nuclear clustering," *Physics Letters B* **755**, 275–278 (2016).
- <sup>24</sup>F. e. a. Negoita, "Laser driven nuclear physics at eli-np," *Romanian Reports in Physics* **68**, S37 (2016).
- <sup>25</sup>A. J. Koning, S. Hilaire, and M. C. Duijvestijn, "TALYS-1.0," in *Proceedings of the International Conference on Nuclear Data for Science and Technology*, Vol. 211, edited by O. Bersillon, F. Gunsing, E. Bauge, R. Jacqmin, and S. Leray (EDP Sciences, 2008) p. 058.
- <sup>26</sup>A. J. Koning and D. Rochman, "Modern Nuclear Data Evaluation with the TALYS Code System," *Nucl. Data Sheets* **113**, 2841 (2012).
- <sup>27</sup>P.-A. Söderström, C. Matei, L. Capponi, E. Açıksoz, D. L. Balabanski, and I. O. Mitu, "Characterization of a plutonium-beryllium neutron source," *Appl. Radiat. Isot.* **167**, 109441 (2021).
- <sup>28</sup>L. Swiderski, M. Moszyński, W. law Czarnacki, J. Iwanowska, A. Syntfeld-Każuch, T. Szczęśniak, G. Pausch, C. Plettner, and K. Roemer, "Measurement of Compton edge position in low-Z scintillators," *Radiat. Meas.* **45**, 605 (2010).
- <sup>29</sup>J.-L. Dubois, F. Lubrano-Lavaderci, D. Raffestin, J. Ribolzi, J. Gazave, A. C. L. Fontaine, E. d'Humières, S. Hulin, P. Nicolaï, A. Poyé, and V. T. Tikhonchuk, "Target charging in short-pulse-laser-plasma experiments," *Phys. Rev. E* **89**, 013102 (2014).
- <sup>30</sup>B. Martinez, E. d'Humières, and L. Gremillet, "Synchrotron radiation from ultrahigh-intensity laser-plasma interactions and competition with bremsstrahlung in thin foil targets," *Phys. Rev. Research* **2**, 043341 (2020).
- <sup>31</sup>M. Janecek, "Reflectivity spectra for commonly used reflectors," *IEEE Transactions on Nuclear Science* **59**, 490–497 (2012).
- <sup>32</sup>P. Bolton, M. Borghesi, C. Brenner, D. Carroll, C. De Martinis, F. Fiorini, A. Flacco, V. Floquet, J. Fuchs, P. Gallegos, D. Giove, J. Green, S. Green, B. Jones, D. Kirby, P. McKenna, D. Neely, F. Nuesslin, R. Prasad, S. Reinhardt, M. Roth, U. Schramm, G. Scott, S. Ter-Avetisyan, M. Tolley, G. Turchetti, and J. Wilkens, "Instrumentation for diagnostics and control of laser-accelerated proton (ion) beams," *Physica Medica* **30**, 255–270 (2014).
- <sup>33</sup>S. R. Mirfayzi, S. Kar, H. Ahmed, A. G. Krygier, A. Green, A. Alejo, R. Clarke, R. R. Freeman, J. Fuchs, D. Jung, A. Kleinschmidt, J. T. Morriison, Z. Najmudin, H. Nakamura, P. Norreys, M. Oliver, M. Roth, L. Vassura, M. Zepf, and M. Borghesi, "Calibration of time of flight detectors using laser-driven neutron source," *Review of Scientific Instruments* **86**, 073308 (2015), <https://doi.org/10.1063/1.4923088>.